CHANGING THE BOUNDARY CONDITIONS: FROM WALLS TO AIR-WATER INTERFACES

R. Jason Hearst
Department of Energy and Process Engineering
Norwegian University of Science and Technology
7034 Trondheim, Norway
jason.hearst@ntnu.no

ABSTRACT

Canonical turbulent flows are typically studied with idealised inlet and boundary conditions, yet environmental and engineering flows are often exposed to external turbulence and deformable interfaces. Herein, three examples are considered in which active grids are used to vary the incoming turbulence while holding other principal forcing parameters approximately fixed. In this way, the boundary conditions of the problem are changed and their effects can be investigated. First, freestream turbulence imposed above a solid-wall turbulent boundary layer is shown to increase the friction velocity and boundary layer thickness while leaving the near-wall cycle and logarithmic region comparatively intact. Second, controlled sub-surface turbulence is shown to enhance air–water mass transfer even when the mean water velocity is unchanged. For small, non-breaking capillary waves, the transfer rate is governed more strongly by bulk turbulence than by measurable surface topology. Finally, measurements of airflow over water demonstrate that sufficiently strong air-side freestream turbulence alters the wave field, a feature that is typically not considered in ocean modelling. Once the velocity deficit associated with the temporally varying rough surface is accounted for, canonical logarithmic behaviour is recovered outside the wave-affected near-interface region. Together, these results illustrate how controlled changes to inlet and boundary conditions expose coupling mechanisms that are absent from idealised canonical configurations.

INTRODUCTION

Traditionally in turbulence, we consider "canonical" flow problems. These are benchmark problems against which theories are tested and models for computational fluid dynamics are established. Examples include turbulent boundary layers, homogeneous isotropic turbulence, and free shear flows. Typically, we investigate these flows with idealised inlet and boundary conditions, e.g., a laminar freestream over a solid wall. These configurations allow us to probe the nature of turbulent flows and establish reliable baselines for comparison across facilities, theories, and computations. However, these idealised scenarios rarely exist in the real world. For instance, in the atmospheric boundary layer it is common that freestream turbulence (FST) exists above the boundary layer.

Herein, we explore the effects of changing the boundary conditions in three problems. First, we consider the influence of FST on a solid-wall turbulent boundary layer (Figure 1(a)). Next, the solid wall is replaced by a gas–liquid (air–water) interface, and we examine how changing the incoming liquid-phase turbulence affects mass transfer (Figure 1(b)). Finally, airflow with varied FST over water is used to investigate the boundary layer that develops above the interface and the resulting surface deformations (Figure 1(c)).

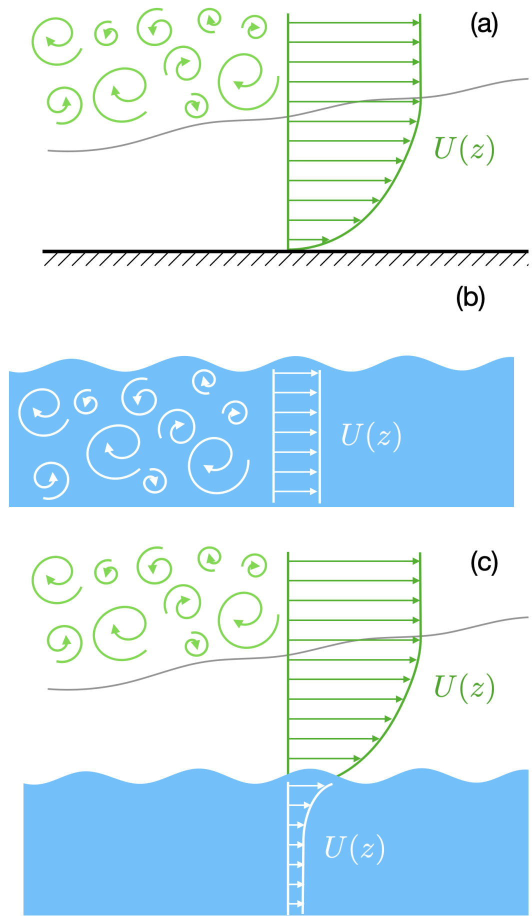

Figure 1. Schematic representations of flows with altered boundary conditions: (a) a turbulent boundary layer with freestream turbulence above it; (b) water flowing with freestream turbulence added upstream; (c) air with freestream turbulence flowing above a gas–liquid interface. The illustrated vortical structures represent where the turbulent forcing is applied.

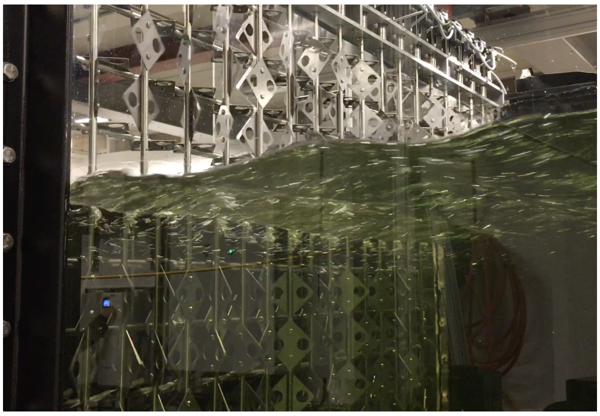

Figure 2. Two-phase active grid at the Norwegian University of Science and Technology.

ACTIVE GRIDS

The three scenarios considered here share a common feature: controlled FST is added to each. Traditionally, this was done in mean flow facilities with passive grids, e.g., Hancock & Bradshaw (1983, 1989). In such a set-up, the flow passes through a grid, and the wakes of the individual bars evolve downstream, eventually meeting, and producing turbulence that is homogeneous in transverse planes and roughly isotropic. The limitation of this approach is that it is relatively limited in the achievable Taylor microscale Reynolds numbers, $Re_\lambda = u'\lambda/\nu$, that can be achieved; where u' is the standard deviation of the velocity fluctuations, λ is the Taylor microscale and ν is the kinematic viscosity. Passive grid studies are largely limited to $Re_\lambda \lesssim 100$, although exceptions exist, e.g., Sinhuber *et al.* (2015).

To overcome this limitation, Makita (1991) developed his "active grid," see Figure 2. This is a device that consists of a series of rods, separated by a distance M, that are actuated by stepper motors. Each rod has a series of square wings mounted to it. By actuating the rods with a predetermined randomised sequence with set parameters, one can adjust the Re_λ of the turbulence produced in the wake of the grid, and correspondingly the turbulence intensity (u'/U, where U is the mean velocity), and the length scales (Larssen & Devenport, 2011; Hearst & Lavoie, 2015). Such an approach is used here to produce approximately homogeneous and isotropic turbulence at different Re_λ and u'/U.

In principle, it is also possible to use active grids to make more creative flows. For instance, they can produce custom gusts (Neuhaus *et al.*, 2021) or adjustable shear flows with independently controllable turbulence intensity (Hearst & Ganapathisubramani, 2017). However, for the purpose of the present investigation, we desired homogeneous flows. For more details on active grids in general and what we have learned about turbulence from them, see the review by Hearst *et al.* (2027).

TURBULENT BOUNDARY LAYERS SUBJECTED TO FREESTREAM TURBULENCE

One physically relevant example in which altered boundary conditions have provided unique insight is the influence of freestream turbulence on a turbulent boundary layer (TBL). As previously mentioned, such set-ups were typically limited by low Re_λ as a result of passive grids being used to generate the turbulence, e.g., Hancock & Bradshaw (1983, 1989). Active grids were introduced to this area by Sharp *et al.* (2009) who placed a boundary layer plate downstream of an active grid in their wind tunnel. With this they were able to increase their Reynolds number to $Re_\lambda = 550$. From this and a series of subsequent experiments by others (e.g., Dogan *et al.*, 2016, 2017; Esteban *et al.*, 2017) it has become clear that increasing Re_λ or u'/U at a fixed freestream velocity, U_∞, increases the friction velocity, U_τ, and the boundary layer thickness, δ, thereby also increasing friction Reynolds number, $Re_\tau = U_\tau\delta/\nu$, which is the representative Reynolds number for wall-bounded flows. In fact, Dogan *et al.* (2017) even suggest that this is a means of artificially increasing Re_τ in standard-sized facilities as the broad characteristics of the near-wall cycle appear to be preserved.

The measurements of Jooss *et al.* (2021), reproduced in Figure 3, illustrate both the effect of changing the freestream conditions and the subsequent downstream evolution. Even at $Re_\lambda = 725$ and $Re_\tau = 5060$, the mean profiles retain a recognisable viscous sublayer (where $U^+ = z^+$) and logarithmic region (Figure 3(a)–(c)); the latter is traditionally given by,

$$U^+ = \frac{1}{\kappa}\ln z^+ + B, \tag{1}$$

where $U^+ = U/U_\tau$, $z^+ = zU_\tau/\nu$, κ is the von Kármán constant, and B is an additive constant. The main departure from the canonical profile occurs farther from the wall, where FST reduces the wake component and produces a profile resembling that of a boundary layer under a favourable pressure gradient. Downstream, the wake gradually recovers as the boundary layer grows while the imposed FST decays. The variance profiles respond more strongly (Figure 3(d)–(f)). Without appreciable FST, the near-wall peak increases downstream in the expected manner (Figure 3(d)). At moderate FST ($u'/U = 7.4\%$ and initially $Re_\lambda = 303$), outer forcing increases the value of the near-wall peak (Dogan *et al.*, 2016), after which its magnitude remains nearly unchanged as the two flows and their competing effects evolve (Figure 3(e)). For the strongest and largest-scale FST ($u'/U = 12.5\%$ and initially $Re_\lambda = 725$), the near-wall peak instead decreases downstream (Figure 3(f)). In this sense the boundary layer can appear to *devolve*: its turbulent energy diminishes with streamwise distance even though Re_τ continues to increase. This is an unusual result that has only been illuminated through the severe adjustments to the boundary and inlet conditions achievable via the active grid.

Across the available FST-TBL experiments, two features persist over a surprisingly broad parameter range. The first is the inner spectral peak associated with the near-wall cycle (c.f., Hutchins & Marusic, 2007). As shown in Figure 4(a), its location remains comparatively insensitive to external forcing. FST can increase U_τ, but the added energy appears mainly at wavelengths larger than those associated with the autonomous near-wall cycle. The second feature concerns the outer length scale. Figure 4(b) combines measurements from Sharp *et al.* (2009), Dogan *et al.* (2016), Hearst *et al.* (2018), and Jooss *et al.* (2021), covering three facilities, air and water flows, different diagnostics, and multiple downstream locations. In all cases, the freestream pre-multiplied spectrum peaks near $\lambda_x \approx 10\delta$, where λ_x is wavelength in the x-direction. If that wavelength is used as an estimate of the freestream integral scale, the data imply an approximate proportionality $L/\delta \approx 10$. The combined evidence therefore suggests a useful separation of roles: the FST level primarily influences U_τ, whereas its large-scale content constrains the resulting boundary-layer thickness.

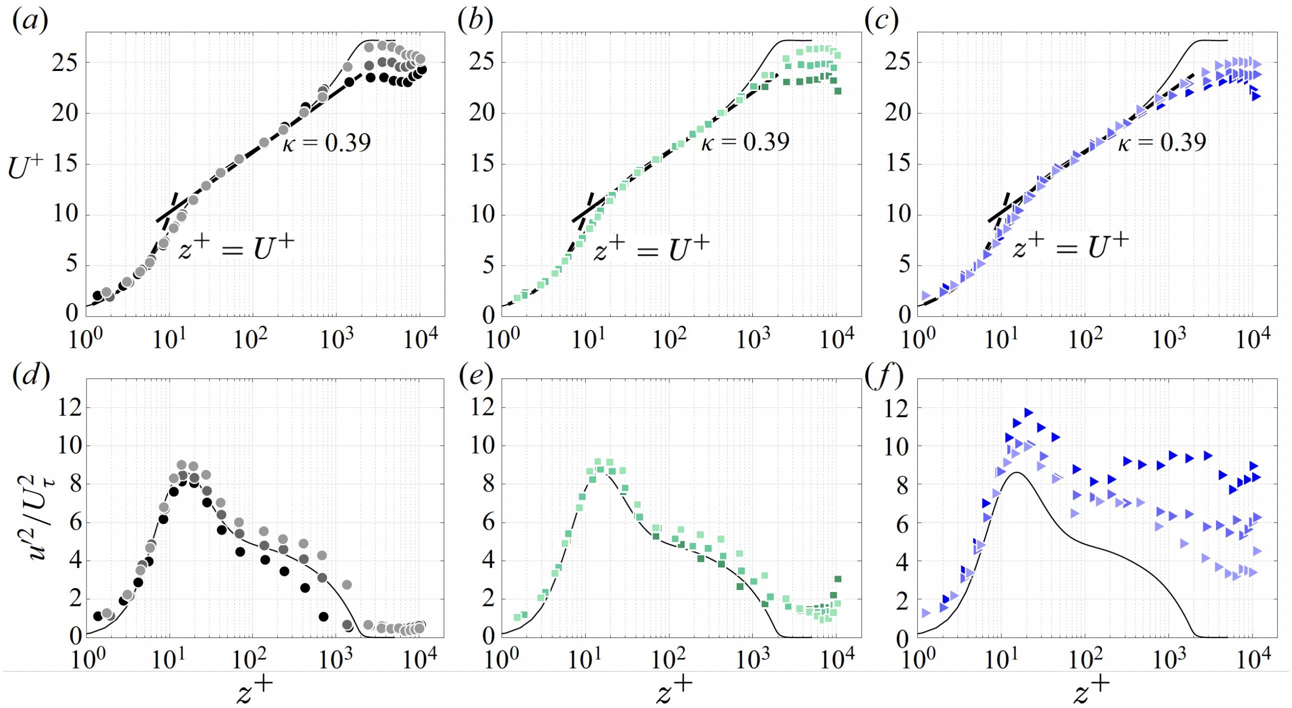

Figure 3. Evolution of a turbulent boundary layer subject to freestream turbulence. (a-c) Mean velocity profiles and corresponding (d-f) variance profiles. Decreasing darkness represents increasing downstream positions of $x/M = 35$, 55 and 95 from the grid. The freestream Re_λ at the first measurement station are (a,d) 59, (b,e) 176 and (c,f) 725. The solid lines are reference DNS from Sillero *et al.* (2013). The von Kármán constant is κ, z is the wall-normal direction, and $\cdot^+$ represents normalisation by viscous units, i.e., U_τ and ν. Adapted from Jooss *et al.* (2021).

The central role of wall shear and the universality of the near-wall spectral peak provide a useful connection to the work of Fukagata *et al.* (2002); the senior author of this work is Nobuhide Kasagi, the namesake for the TSFP Kasagi Award. The exact decomposition of Fukagata *et al.* (2002) expresses skin friction as contributions from laminar transport, the Reynolds stress distribution, streamwise inhomogeneity, and unsteadiness. For a statistically steady, approximately zero-pressure-gradient TBL, the turbulent contribution is a weighted integral of the Reynolds shear stress, with the near-wall region carrying particular importance. The FST experiments discussed here can therefore be viewed not only as changes to the mean velocity profile, but as controlled modifications to the Reynolds stress distribution that ultimately set U_τ. The persistence of the near-wall spectral cycle does not imply unchanged skin friction; additional Reynolds stress at larger scales can still increase the integrated momentum transport to the wall.

TURBULENCE-ENHANCED MASS TRANSFER

We now consider a second change to the boundary condition by replacing the solid wall with a free surface. This introduces a new class of problems, one of which is mass transfer across a gas–liquid, specifically air–water, interface. Mass transfer, also commonly referred to as gas transfer, describes the exchange of gaseous species across the interface as the two phases approach equilibrium. A prominent example is the exchange of CO_2 between the atmosphere and the oceans; the latter absorb approximately 25% of annual anthropogenic CO_2 emissions (DeVries, 2022). Substantial uncertainty nevertheless remains in the rates and mechanisms governing this exchange.

When both fluids are quiescent, the transfer is governed primarily by the concentration or partial-pressure difference across the interface and by molecular diffusion. Flow, turbulence, waves, bubbles and droplets introduce additional mechanisms (Deike, 2022). Surface deformation can alter the interfacial geometry, while vortical motions beneath the surface continually transport dissolved gas away from the interface and replace it with unsaturated liquid. This latter picture is closely related to the surface-renewal concept, in which the gas-transfer velocity depends on how rapidly sub-surface motions replenish the thin concentration boundary layer.

To further link this to the previous work of Kasagi, the connection between near-boundary turbulence and scalar transport was evident in his previous DNS (Kasagi *et al.*, 1992). For a passive scalar in turbulent channel flow, Kasagi *et al.* (1992) found that near-wall temperature fluctuations were strongly correlated with streamwise velocity fluctuations and that the budgets of turbulent heat flux closely resembled those of the corresponding Reynolds stresses. Although an air–water interface differs fundamentally from a no-slip solid wall, the broader lesson is directly relevant here: momentum and scalar transport are organised by related near-boundary turbulent motions. At a free surface, these motions govern how rapidly gas-enriched liquid is carried into the bulk and replaced by unsaturated fluid.

In quiescent tanks, Herlina & Jirka (2008) and Variano & Cowen (2013) demonstrated that turbulence changes the transfer rate of sparingly soluble gases. In flowing systems, where much of the kinetic energy resides in the mean flow, the importance of turbulence relative to surface deformation and mean transport was less clear. Bullee *et al.* (2024) varied the incoming turbulence with an active grid while maintaining an approximately constant mean velocity and found that the gas-

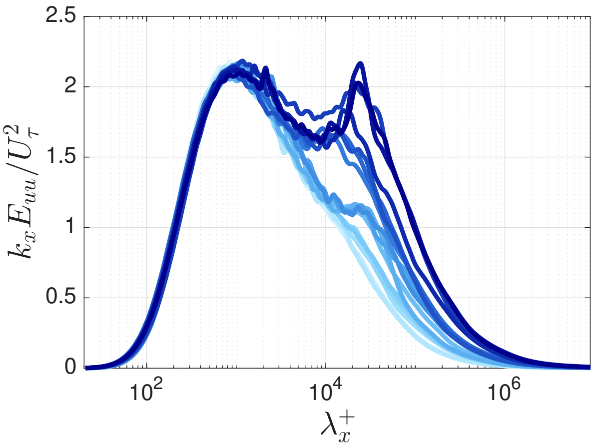

(a)

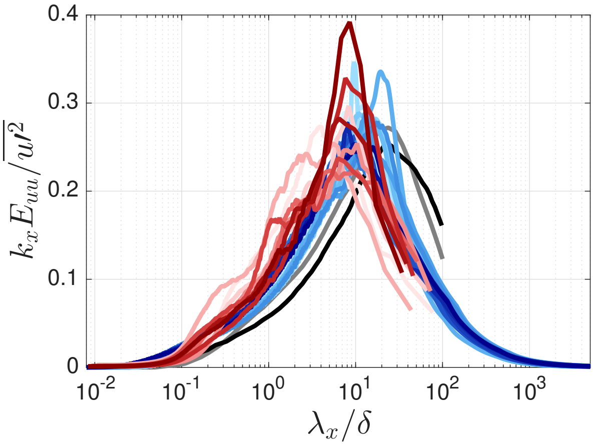

(b)

Figure 4. Pre-multiplied velocity spectra at (a) the near-wall peak ($z^+ \approx 15$), and (b) in the freestream. Blue data is from Hearst *et al.* (2018) with $1890 \leq Re_\tau \leq 5360$ and $302 \leq Re_\lambda \leq 760$. Red data is from Jooss *et al.* (2021) with $1210 \leq Re_\tau \leq 5060$ and $45 \leq Re_\lambda \leq 725$. Black data is from Sharp *et al.* (2009) with $680 \leq Re_\tau \leq 2020$ and $20 \leq Re_\lambda \leq 550$. For all cases, increasing darkness represents increasing FST intensity. Note, some of the data from Hearst *et al.* (2018) first appeared in Dogan *et al.* (2016, 2017).

transfer velocity increased with turbulence intensity, with an enhancement of approximately 15%, aligned with the general scalar transport expectations from Kasagi *et al.* (1992).

Li *et al.* (2025) subsequently separated the effects of sub-surface turbulence and non-breaking capillary waves by combining an active grid with an array of surface-penetrating dowels. The dowels generated capillary waves, while their penetration depth and the active-grid state allowed similar surface conditions to be produced with different bulk turbulence levels, and vice versa. Across their five cases, the gas transfer velocity showed no clear relationship with the mean-square surface slope or the small increase in surface area. By contrast, it correlated strongly with the bulk turbulence intensity integrated over the water column, even though that turbulence was generated by different mechanisms. Over the tested range, the transfer velocity increased by 45%. These results indicate that, in the non-breaking capillary-wave regime, sub-surface turbulence rather than the measured surface topology controls the gas-transfer rate.

The corresponding oxygen reaeration histories are shown

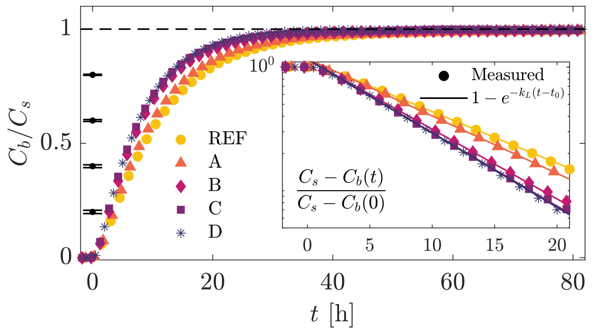

Figure 5. Normalised bulk concentration (C_b) of dissolved O_2 in water measured by Li *et al.* (2025). Increasing symbol darkness represents increasing bulk turbulence intensity. The saturation concentration is C_s. The dissolved O_2 concentration approaches saturation in all cases, but the rate varies with the turbulence level. The inset identifies the region fitted by $1 - \exp[-k_L(t - t_0)]$. The error bars on the left represent the worst case RMS variations over a 15-minute temporal averaging window at different C_b/C_s values.

in Figure 5. The Schmidt numbers, $Sc = \nu/D$, where D is the molecular diffusivity, of O_2 and CO_2 in water are of the same order, $\mathcal{O}(500)$, although their solubilities differ. This means that, after the species cross the gas-liquid interface, their transport within the liquid phase is governed by comparable ratios of momentum to molecular diffusivity. O_2 is commonly measured in the laboratory because the air in the lab acts as a (relatively) infinite source of O_2 and there are comparatively few health and safety concerns with its use. Following Li *et al.* (2025), the data between $0.2 \leq C_b/C_s \leq 0.8$ are fitted by

$$\frac{C_b}{C_s} = 1 - \exp\left[-k_L(t - t_0)\right], \tag{2}$$

where C_b is the bulk dissolved oxygen concentration, C_s is its saturation value, and k_L and t_0 are fitting parameters. The gas-transfer velocity is then obtained from $k = k_L V/A$, where V is the water volume and A is the exposed interfacial area. The steeper concentration histories at higher bulk turbulence levels therefore correspond to larger gas transfer velocities, k.

These measurements quantify the bulk mass transfer rate, but not the instantaneous mechanisms responsible for it. To understand the mechanisms, one must be able to measure and quantify the events that are responsible for the mass transfer. To accomplish this, Herlina & Jirka (2008) developed a laser-induced fluorescence technique that enabled them to measure the instantaneous, spatial distribution of dissolved O_2 in water. Simultaneous measurements of the instantaneous concentration and velocity fields, the latter obtained by particle image velocimetry, allow the turbulent scalar fluxes to be evaluated. The approach of Herlina & Jirka (2008) was developed for quiescent flow beneath a flat interface. Most flows of interest have deformable interfaces. As such, Shankaran & Hearst (2025) adapted the technique for advecting, deformable interfaces. An example of this approach is presented in Figure 6, where a vortical event transports part of the high-concentration diffusive layer near the surface into the bulk. While the investigations with this technique are ongoing, these images and the existing results presented by Shankaran & Hearst (2025) demonstrate that the fluxes are dependent on where one is in the reaeration curve, i.e., Figure 5. This has consequences

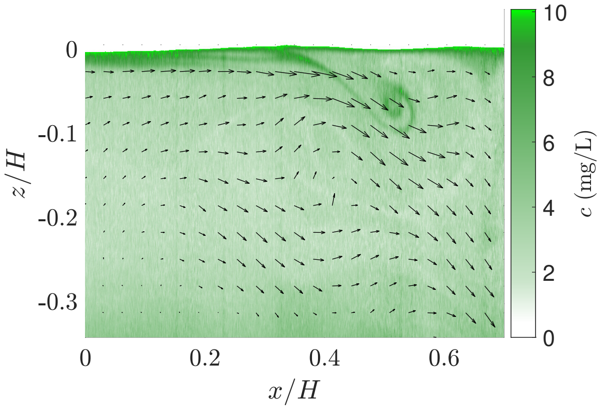

Figure 6. Example of an instantaneous field of dissolved O_2 measured with laser induced fluorescence with superimposed velocity vectors from particle image velocimetry. The bulk air velocity is 4.58 m/s, which generates low amplitude interfacial waves. Adapted from Shankaran & Hearst (2025).

for the design and interpretation of experiments because many laboratory studies focus on low saturation levels, whereas natural waters often operate much closer to saturation. The absolute flux and the relative importance of individual transport events can therefore differ between these conditions.

FREESTREAM TURBULENCE AND GAS-LIQUID INTERFACES

Combining the two previous scenarios, we arrive at a situation where a turbulent boundary layer subjected to FST is evolving over a gas-liquid interface. The gas-phase flow generates waves that act as a mobile roughness and modify the turbulent boundary layer developing above the interface. The key question is whether adding FST produces a measurable change at the gas-liquid interface. Existing evidence is mixed. Experiments with grid-generated turbulence above a gas–liquid interface have suggested that turbulence characteristics have little influence and that the mean velocity is the principal driver (Takagaki *et al.*, 2020). However, this contrasts with what has been observed for solid wall boundary layers, where U_τ grows with the FST intensity. Because interfacial stress contributes directly to wave growth, one might nevertheless expect increasing FST to modify the surface response, despite the findings of Takagaki *et al.* (2020).

In Figure 7, two snapshots of the air-water interface are presented for the same mean flow velocity, $U \approx 4$ m/s, but different FST conditions. The two surfaces are visibly different: the lower image contains sharper and more regular crests and corresponds to the higher turbulence intensity. Thus, sufficiently energetic FST appears capable of modifying the surface response.

The corresponding wave-following mean velocity profiles are shown in Figure 8. For a hydraulically smooth wall, the logarithmic law is given by equation (1). However, a rough or deformable interface produces a downward shift in the logarithmic profile that is represented by the roughness function ΔU^+,

$$U^+ = \frac{1}{\kappa} \ln z^+ + B - \Delta U^+, \qquad (3)$$

or, equivalently, by plotting $U^+ + \Delta U^+$ against z^+. Once this fitted shift is applied, the profiles collapse through much of the

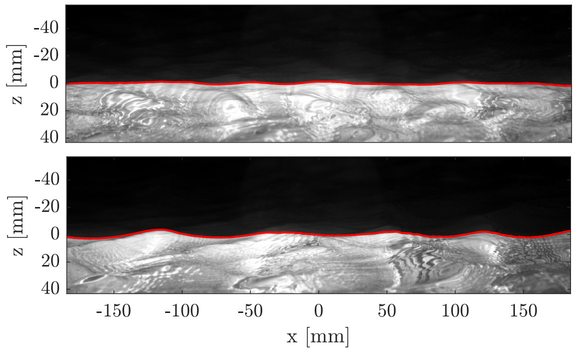

Figure 7. Instantaneous images of a water surface subjected to flowing air above it. The mean freestream air velocity in both images is $U_\infty \approx 4$ m/s. The two images differ only in freestream turbulence intensity, where the top figure has $u'/U = 2.83\%$ and the bottom has $u'/U = 4.82\%$. Even this modest change results in an obvious impact on the surface topology.

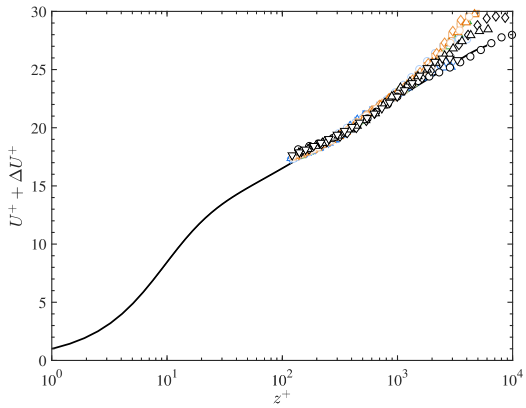

Figure 8. Wave-following boundary-layer profiles normalised in viscous units of flowing air over water. The vertical coordinate, z, is measured from the instantaneous interface and the velocity is shifted by the fitted roughness function, ΔU^+. Increasing darkness represents decreasing turbulence intensity. The DNS data of Graham *et al.* (2016) are included for reference.

logarithmic region and remain close to the canonical smooth-wall reference. The remaining departure nearest the interface occurs within the wave-affected roughness sublayer, where the moving boundary, wave-coherent stresses, and possible sheltering or critical-layer dynamics are expected to matter directly. This region is omitted from Figure 8 because wave motion makes the available velocity samples spatially intermittent. As for the solid-wall TBL, increasing FST primarily modifies the outer part of the mean profile where the wake region is suppressed by FST.

CONCLUSIONS

Canonical configurations remain indispensable because they isolate mechanisms and provide common reference states. The examples considered here show, however, that deliberately changing inlet and boundary conditions can reveal behaviour that is equally systematic. For a solid-wall TBL, FST increases the wall shear and boundary layer thickness while the logarithmic region and the spectral signature of the near-wall cycle remain comparatively robust. The measurements further suggest that the turbulence intensity and the large-scale content of the freestream play distinguishable roles in setting U_τ and δ, respectively.

Replacing the wall with an air-water interface introduces both scalar transport and two-way coupling with a deformable boundary. Controlled water-side turbulence can change the gas-transfer velocity substantially without changing the mean flow velocity, and, for the non-breaking capillary-wave conditions tested, bulk turbulence provides a more consistent scaling than the measured surface topology. On the air side, sufficiently strong FST modifies the wave field and suppresses the outer wake of the surface boundary layer. Nevertheless, after accounting for the roughness function of the transient and deformable interface, the logarithmic portion of the velocity profile remains close to its canonical form. These observations point to a broader conclusion: altered boundary conditions do not simply destroy canonical behaviour. Instead, they identify which parts of that behaviour are robust, which respond directly to external forcing, and which require new descriptions of interfacial coupling.

Acknowledgements

On the occasion of receiving the TSFP Kasagi Award, I would like to acknowledge the support I have received over the years from my previous supervisors and mentors. Prof. Philippe Lavoie at the University of Toronto introduced me to turbulence research and helped shape the path I have followed since beginning my PhD. Prof. Bharath Ganapathisubramani fostered further growth and my time with him confirmed that I wanted to pursue an academic career. Prof. James Dawson welcomed me to NTNU and has been a valuable mentor and collaborator, and has been essential to building what we have at NTNU today.

I would also like to acknowledge the invaluable work of the masters and PhD students, as well as postdoctoral researchers and other academics with whom I have been fortunate to work thus far in my career. The results presented herein are in fact a summary of the work of a broad team of scientists. While I hope that I have not missed anyone, the direct contributions to the work summarised here have come from Prof. Tania Bracchi, Dr. Pim Bullee, Dr. Eda Dogan, Youssef Elashmawi, Prof. Simen Ellingsen, Dr. Yannick Jooss, Dr. Leon Li, Adharsh Shankaran, and Dr. Srikar Yadala.

Funding

Funded by the European Union (ERC StG 101041000, GLITR). Views and opinions expressed are, however, those of the author only and do not necessarily reflect those of the European Union or the European Research Council. Neither the European Union nor the granting authority can be held responsible for them.

REFERENCES

Bullee, P. A., Weichert, S., Nore, A., Li, L., Ellingsen, S. Å. & Hearst, R. J. 2024 The influence of water turbulence on surface deformations and the gas transfer rate across an air-water interface. *Exp. Fluids* **65**, 132.

Deike, L. 2022 Mass transfer at the ocean-atmosphere interface: The role of wave breaking, droplets, and bubbles. *Annu. Rev. Fluid Mech.* **54**, 191–224.

DeVries, T. 2022 The ocean carbon cycle. *Ann. Rev. Environ. Resour.* **47**, 317–341.

Dogan, E., Hanson, R. & Ganapathisubramani, B. 2016 Interactions of large-scale free-stream turbulence with turbulent boundary layers. *J. Fluid Mech.* **802**, 79–107.

Dogan, E., Hearst, R. J. & Ganapathisubramani, B. 2017 Modelling high Reynolds number wall-turbulence interactions in laboratory experiments using large-scale free-stream turbulence. *Phil. Trans. R. Soc. A* **375** (2089), 20160091.

Esteban, L. B., Dogan, E., Rodríguez-López, E. & Ganapathisubramani, B. 2017 Skin-friction measurements in a turbulent boundary layer under the influence of free-stream turbulence. *Exp. Fluids* **58** (9), 115.

Fukagata, K., Iwamoto, K. & Kasagi, N. 2002 Contribution of Reynolds stress distribution to the skin friction in wall-bounded flows. *Phys. Fluids* **14** (11), L73–L76.

Graham, J., Kanov, K., Yang, X. I. A., Lee, M., Malaya, N., Lalescu, C. C., Burns, R., Eyink, G., Szalay, A., Moser, R. D. & Meneveau, C. 2016 A web services accessible database of turbulent channel flow and its use for testing a new integral wall model for LES. *J. Turbul.* **17** (2), 181–215.

Hancock, P. E. & Bradshaw, P. 1983 The effect of free-stream turbulence on turbulent boundary layers. *J. Fluids Eng.* **105**, 284–289.

Hancock, P. E. & Bradshaw, P. 1989 Turbulence structure of a boundary layer beneath a turbulent free stream. *J. Fluid Mech.* **205**, 45–76.

Hearst, R. J., Dogan, E. & Ganapathisubramani, B. 2018 Robust features of a turbulent boundary layer subjected to high-intensity free-stream turbulence. *J. Fluid Mech.* **851**, 416–435.

Hearst, R. J. & Ganapathisubramani, B. 2017 Tailoring incoming shear and turbulence profiles for lab-scale wind turbines. *Wind Energ.* **20**, 2021–2035.

Hearst, R. J., Hölling, M. & Obligado, M. 2027 Physical insights from active grid turbulence. *Annu. Rev. Fluid Mech.* **59** (to appear).

Hearst, R. J. & Lavoie, P. 2015 The effect of active grid initial conditions on high Reynolds number turbulence. *Exp. Fluids* **56** (10), 185.

Herlina & Jirka, G. H. 2008 Experiments on gas transfer at the air-water interface induced by oscillating grid turbulence. *J. Fluid Mech.* **594**, 183–208.

Hutchins, N. & Marusic, I. 2007 Evidence of very long meandering features in the logarithmic region of turbulent boundary layers. *J. Fluid Mech.* **579**, 1–28.

Jooss, Y., Li, L., Bracchi, T. & Hearst, R. J. 2021 Spatial development of a turbulent boundary layer subjected to freestream turbulence. *J. Fluid Mech.* **911**, A4.

Kasagi, N., Tomita, Y. & Kuroda, A. 1992 Direct numerical simulation of passive scalar field in a turbulent channel flow. *J. Heat Transfer* **114**, 598–606.

Larssen, J. V. & Devenport, W. J. 2011 On the generation of large-scale homogeneous turbulence. *Exp. Fluids* **50**, 1207–1223.

Li, L., Bullee, P. A., Ellingsen, S. Å. & Hearst, R. J. 2025 Subsurface turbulence or non-breaking capillary waves: which dominates air-water gas transfer? *J. Fluid Mech.* **1009**, A48.

Makita, H. 1991 Realization of a large-scale turbulence field in a small wind tunnel. *Fluid Dyn. Res.* **8**, 53–64.

Neuhaus, L., Berger, F., Peinke, J. & Hölling, M. 2021 Exploring the capabilities of active grids. *Exp. Fluids* **62**, 130.

Shankaran, A. & Hearst, R. J. 2025 Simultaneous measurements of velocity, oxygen concentration, and deformed interface position in an air-water channel using PIV and LIF. *Exp. Fluids* **66**, 95.

Sharp, N., Neuscamman, S. & Warhaft, Z. 2009 Effects of large-scale free stream turbulence on a turbulent boundary layer. *Phys. Fluids* **21** (095105).

Sillero, J. A., Jiménez, J. & Moser, R. D. 2013 One-point statistics for turbulent wall-bounded flows at Reynolds numbers up to $\delta^+ \approx 2000$. *Phys. Fluids* **25** (105102).

Sinhuber, M., Bodenschatz, E. & Bewley, G. P. 2015 Decay of turbulence at high Reynolds numbers. *Phys. Rev. Lett.* **114** (034501).

Takagaki, N., Suzuki, N., Takahata, S. & Kumamaru, H. 2020 Effects of air-side freestream turbulence on the development of air-liquid surface waves. *Exp. Fluids* **61**, 136.

Variano, E. A. & Cowen, E. A. 2013 Turbulent transport of a high-Schmidt-number scalar near an air-water interface. *J. Fluid Mech.* **731**, 259–287.